INSTITUTE OF PHYSICS PUBLISHING PLASMA PHYSICS AND CONTROLLED FUSION

Plasma Phys. Control. Fusion **46** (2004) 1659–1674 PII: S0741-3335(04)78978-2

Ultrasoft x-ray spectroscopy using multilayer mirrors on TCV

V Piffl[1], H Weisen[2], A Zabolotsky[2] and the TCV Team[2]

[1] Institute of Plasma Physics, Association EURATOM-IPP.CR, Academy of Sciences of the Czech Republic, 182 21 Prague 8, Czech Republic
[2] Centre de Recherches en Physique des Plasmas, Association EURATOM-Suisse Ecole Polytechnique Fédérale de Lausanne, EPFL, 1015 Lausanne, Switzerland

Received 8 April 2004, in final form 17 August 2004
Published 14 September 2004
Online at stacks.iop.org/PPCF/46/1659
doi:10.1088/0741-3335/46/11/001

Abstract

The TCV tokamak is equipped with a four-channel ultrasoft x-ray monochromator allowing low resolution ($\lambda/\Delta\lambda \sim 30$) measurements in the energy range 200–800 eV. Its main purpose is to simultaneously monitor emission from four of the main Kα resonance lines of highly ionized light impurities such as boron, carbon, nitrogen and oxygen. Wavelength selectivity is achieved using synthetic multilayer mirrors having 30–40 alternate layers with layer periods in the range 3–7 nm, depending on the design wavelength range. Recently the instrument was modified for measuring the radial profiles of Kα and Lyman-α lines from He-like and H-like intrinsic carbon impurities to allow estimates of impurity diffusivities by comparisons with simulations using the impurity transport code STRAHL.

(Some figures in this article are in colour only in the electronic version)

1. Introduction

Multilayer mirrors (MLM) made from alternating layers of different reflectivity in the ultrasoft x-ray range (200–1000 eV) offer diagnostic possibilities in a wavelength range outside the reach of most existing spectrometers, such as VUV instruments used at lower energies and x-ray spectrometers used at higher energies. The main resonance lines of hydrogen and helium-like low Z intrinsic impurities, from boron to oxygen, are in this energy range. These elements constitute the majority of the intrinsic impurities in most contemporary tokamaks, and for a device the size of TCV (or larger) more than half of the total radiated power from light impurities is due to line radiation in this spectral range. The use of MLM technology in fusion devices has become fairly widespread [1–9]. The neutron resilience of the mirrors has motivated proposals for their use in a fusion reactor environment [3].

The instrument described in this paper was built to monitor emission from four lines simultaneously and has been used for this purpose for some seven years on TCV. The ionization balance of light impurities is a sensitive function of the electron temperature, electron density

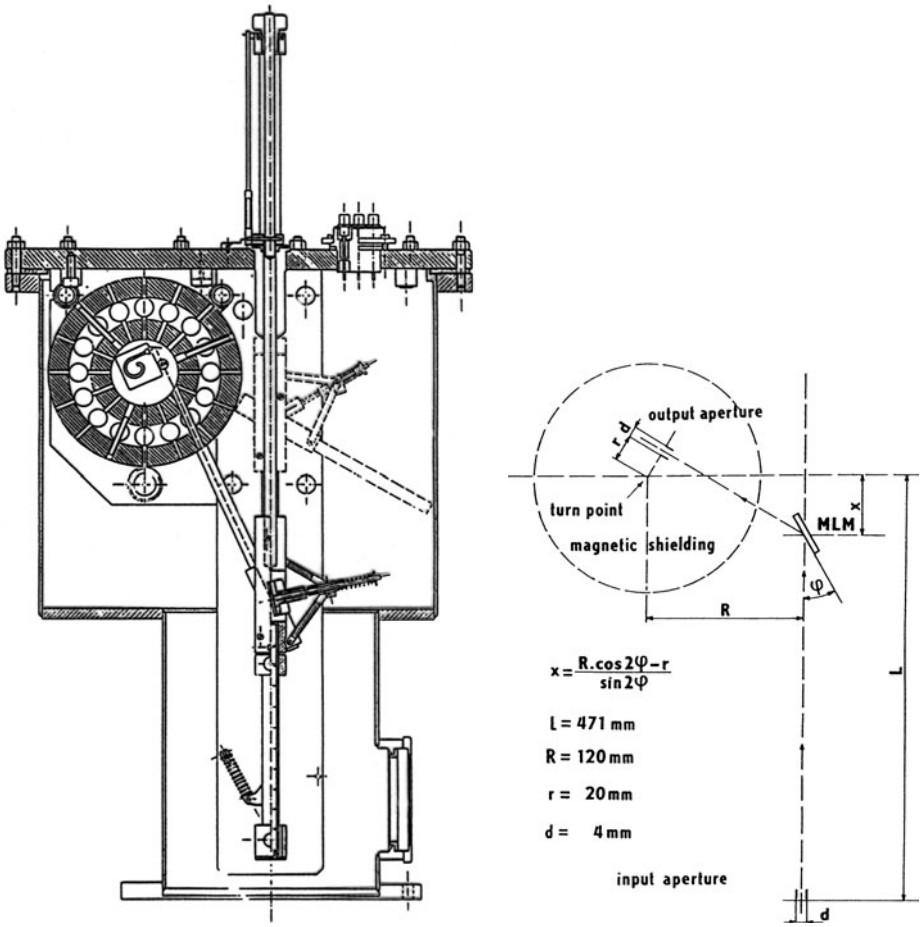

Figure 1. Ultrasoft x-ray multichromator. Left: overall design outline. The channeltrons are represented by the square box in the core of the cylindrical magnetic shielding structure. Separation from the TCV vacuum is achieved by polymer foils placed below the input aperture. Right: ray path geometry.

and the ion transport coefficients just inside the last closed flux surface (LCFS), where the H and He-like ionization stages are most abundant. In a specific set of recent experiments, the spectrometer was equipped for measuring carbon emission profiles. These profiles are compared with simulations from an impurity transport code to obtain estimates of the transport coefficients.

2. Spectrometer design

The spectrometer was designed and fabricated at the IPP Prague and is of the θ–2θ design (figure 1). The centre wavelength of each of the four channels of the device can be independently adjusted, while maintaining alignment, thanks to a pantograph system that mechanically couples the mirror position, the incidence angle as it slides along a guiding rod and the detector orientation. The channeltron detectors are housed in a cylindrical soft iron magnetic shield of total thickness 4 cm, which guards them against the magnetic fields ($\sim$0.1 T, from the Ohmic transformer and the shaping coils) at its location 1.5 m above the TCV vacuum

vessel. The shielding is equipped with cylindrical holes for outgassing and for transmitting the radiation from the MLMs to the channeltron detectors. It rotates together with the detector inside it when the wavelength setting is changed. The residual magnetic fields in the detector area were measured to be as low as 10^{-4} T.

During operation the vacuum of the apparatus ($\sim 10^{-6}$ mbar), established using a small turbomolecular pump, is separated from the TCV vacuum ($\sim 10^{-8}$ mbar) by 0.3 μm thick polymer foils (one for each channel) supported by silicon grids that can withstand a pressure difference in excess of 1 bar and have acceptable transmission in the energy range of interest [10]. We found that transmission of undesirable VUV radiation through the polymer window was significant, as indicated by radiation spikes at breakdown and during plasma termination. Thin ($\sim 0.2\,\mu$m) film metal filters, chosen for the different energy ranges, were therefore inserted between the polymer vacuum window and the entrance aperture of the instrument. The four channels of the device use different mirrors and filters optimized for the ranges 200–300, 300–400, 400–500 and 500–800 eV.

2.1. Multilayer mirrors

MLMs are reflective artificial periodic structures composed of alternating layers of highly reflective materials and low Z spacers. The energy selectivity of the MLMs depends on the number of layer pairs. The flat MLMs used on TCV have 30–50 layer pairs with periods in the range 3–7 nm, depending on their design wavelength range. The incident radiation is diffracted according to the Bragg law, $m\lambda = 2d \sin\theta$. The mirrors used here were custom made at the Institute of Applied Physics, Nizhny Novgorod, Russia. They were supplied along with measurements of their reflectivity (shown in figure 2) and wavelength selectivity. These characteristics were measured at different wavelengths using a grating USX monochromator and the emission from an x-ray tube with exchangeable anodes. The detailed dependence of the mirror parameters on energy has been calculated and fitted to the measured values. The reflectivity in the second order is less then 0.11% for the wavelengths used.

2.2. Filters and windows

Sub-micron metal foils of tin, silver and nickel–carbon composites, supported by two nickel meshes with 0.72% free aperture transmission are used as energy pass band filters to suppress the VUV emission and second order mirror reflections. The foils were produced by laser evaporation at the Ioffe Institute in St Petersburg and their thickness was evaluated by transmission measurements using L- and K-lines of different elements in the relevant energy range (dot-dashed lines in figure 2). It was found that the thickness variation of the filters from the same batch did not exceed 5%. However the long term stability may be a concern, since the filter transmittance may vary as a result of oxidation if the filters are left exposed to oxygen or moisture. The residual transmission of visible light was measured to be less than 10^{-6}. The transmission of the polymer windows is shown as broken lines in figure 2 and was obtained from the manufacturer [10].

2.3. Detector units

Each detector consists of a channeltron and an integrated compact electronics package for charge detection and pulse shaping and is placed at the axis of the spectrometer cylindrical magnetic shielding. The Russian VEU-6 channeltrons used have a gain of 10^6 and are designed for photon count rates of up to 5×10^5 counts s^{-1}. They are equipped with negatively biased

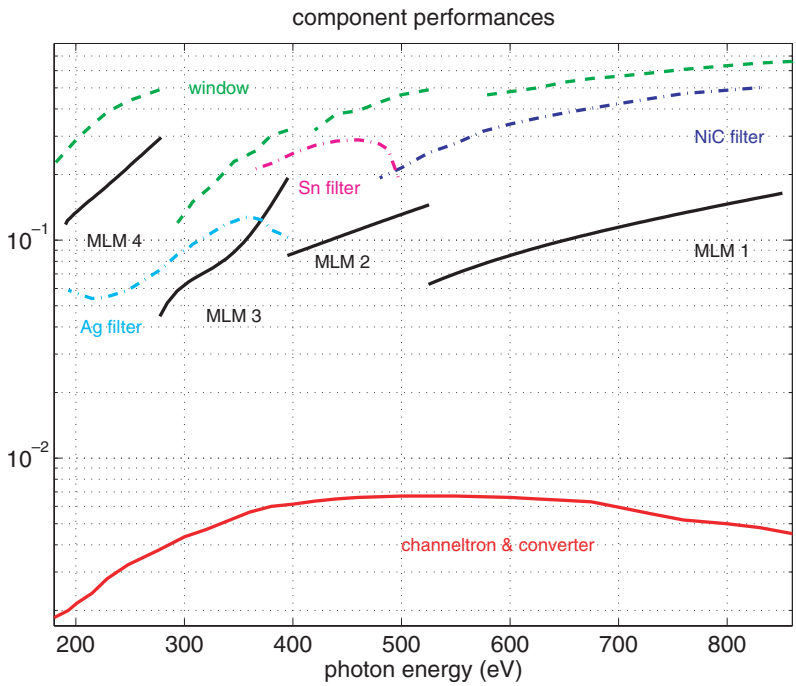

Figure 2. USX spectrometer component performance. - - - -: polymer window transmittance. — · —: filter transmittance. Solid lines labelled MLM1–MLM4: mirror reflectivities. Lower solid line: detection efficiency of channeltrons with photocathode.

front-end tungsten photon-to-electron converters. Although this leads to an approximately four-fold reduction in overall sensitivity compared with an open channeltron, it has the advantage of a uniform response across the detector surface. The detection efficiency of the channeltron with the tungsten photocathode, η, was measured using a USX monochromator and absolutely calibrated electron multiplier with a gold first dynode at the Ioffe Institute (figure 2, lower solid line). The measurements also confirmed that the quantum efficiency of the tungsten converter does not change over the 4 mm diameter sensitive area. The accuracy of the detection efficiency measurements is better than $\pm 35\%$. The main factors that influence the accuracy are systematic dosimetry errors and fluctuations of the x-ray intensity during the measurements.

The custom built electronics consists of a charge sensitive preamplifier, an amplitude discriminator and an output pulse shaping circuit. The input circuits have a nanosecond time resolution and deliver square pulses of +5 V, 0.5 μs duration, for each detected photon. These pulses are transmitted to a multichannel scaler (pulse counting acquisition unit) with adjustable integration time, typically set to 1 ms. The bias voltage between the tungsten converter and the input cone of the channeltron is -400 V. The voltage applied to the channeltron is +3.1 kV. The average undiscriminated dark count rate is 0.1–0.3 counts s^{-1} at room temperature in a vacuum of 10^{-5} mbar.

3. Throughput

The above measurements were interpolated to the energy ranges of interest. The results are summarized in table 1 for the energies corresponding to the Lyman-α lines of hydrogen-like B, C, N and O.

Table 1. Characteristics of spectrometer components at energies of B, C, N and O Lyman-α. E is the line energy, ΔE the MLM bandwidth, d the layer period, θ the Bragg angle, R_{MLM} the MLM reflectivity; T stands for transmission and η is the efficiency of the channeltron–converter combination.

Element	E (eV)	ΔE (eV)	MLM no and pair	$2d$ (Å)	θ (°)	R_{MLM}	T_{window}	Filter	T_{filter}	η
B V	255	15	4-Ni/C	132	21.5	0.23	0.45	Ag	0.057	3.8×10^{-3}
C VI	367	13.9	3-Fe/Sc	90	22	0.12	0.26	Ag	0.125	6.8×10^{-3}
N VII	501	32.5	2-W/Si	107	14	0.133	0.46	Sn	0.28	6.5×10^{-3}
O VIII	654	21.4	1-W/Si	68	16	0.10	0.53	Ni/C	0.39	6.3×10^{-3}

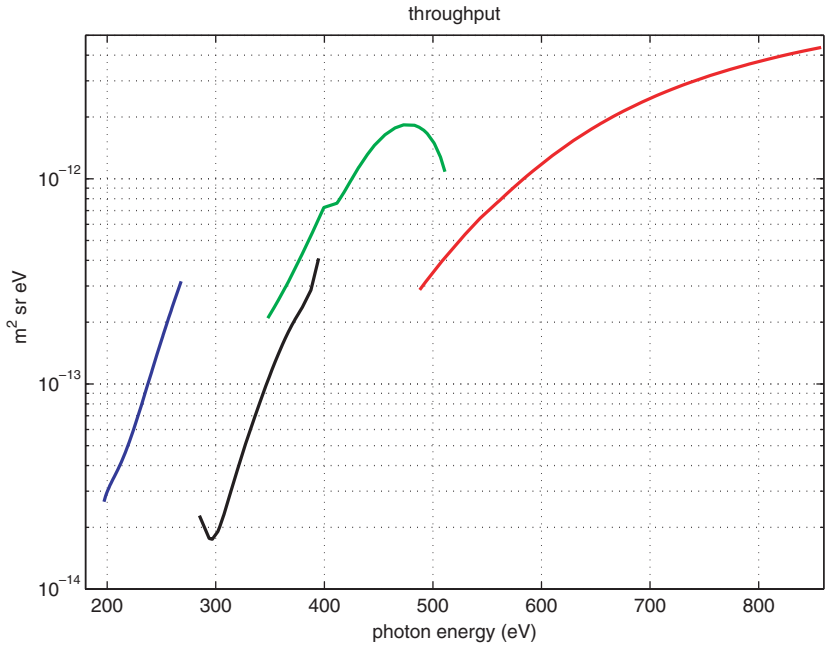

Figure 3. USX spectrometer throughput as a function of photon energy.

The étendue is defined as $A\Omega = A_{\mathrm{o}} A_{\mathrm{i}}/d^2$, where A_{o} and A_{i} are the collimator output and input apertures and d the distance between them along the ray path. This distance varies with the wavelength setting as the MLM slides along its guiding rod (figure 1).

The throughput, defined as

$$\zeta = A\Omega \times T_{\mathrm{window}} \times T_{\mathrm{filter}} \times R_{\mathrm{MLM}} \times \eta_{\mathrm{chan}} \times \Delta E \ (\mathrm{m^2\,sr\,eV})$$

is shown as a function of photon energy in figure 3. (The terms are defined as in table 1). The large variations reflect the energy dependence of the components used, mainly the filters and the vacuum windows. For broadband radiation from an extended source, the count rate, F (pulses $\mathrm{s^{-1}}$), is obtained from $F = \zeta \times \phi$, where ϕ is the spectral brilliance of the radiation source (photons $\mathrm{s^{-1} m^{-2} sr^{-1} eV^{-1}}$). For a single spectral line of width $\Delta E_{\mathrm{l}} \ll \Delta E$, as is the case for most of the observations using this instrument, the count rate is expressed as $F = \zeta/\Delta E \times \Phi$, where Φ is the photon flux from the line (photons $\mathrm{s^{-1}\ m^{-2}\ sr^{-1}}$) and the line brilliance is $E_{\mathrm{l}} \times \Phi$ ($\mathrm{W\,m^{-2}\,sr^{-1}}$), where E_{l} is the energy of the transition. The uncertainty in ζ,

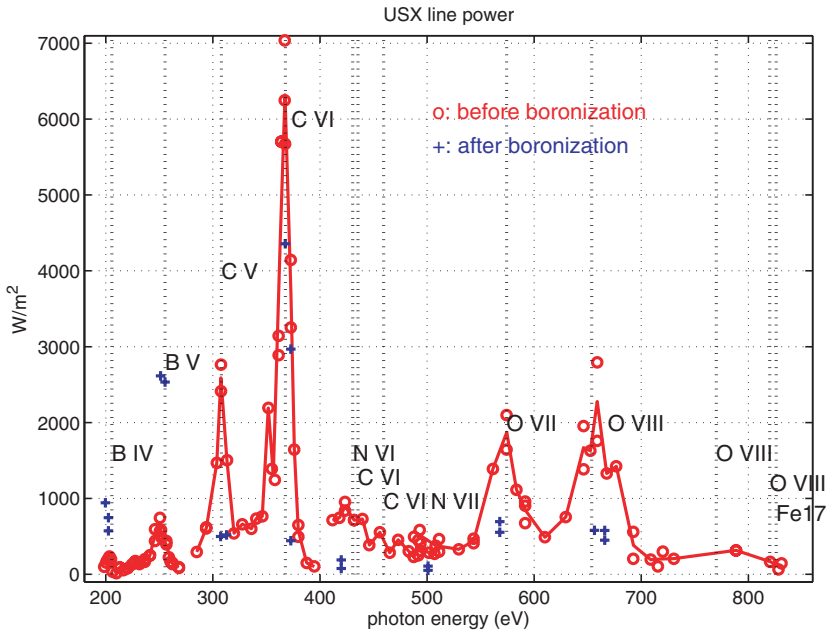

Figure 4. Ultrasoft x-ray spectrum obtained by a shot-to-shot scan of photon energy.

resulting from the cumulated uncertainties of the individual component parameters, is estimated at a factor of 2. Errors in detector sensitivity are estimated at 35% (from manufacturer), filters 10–20% (corresponding to a 5% error on thickness). No data are available for errors in window transmission and mirror reflectivity, but they are not believed to be better than 20%. An additional 20% uncertainty arises for line brilliance measurements due to the adjustment of the centre wavelength by scanning the line over a few tokamak discharges and setting it to the maximum.

4. Survey of light impurity behaviour

The vertically viewing instrument is placed slightly outside the magnetic axis position, with viewing lines crossing the plasma midplane at $r/a \approx 0.4$ on the low field side. This is not a limitation, since most of the radiation investigated originates from the plasma periphery. The instrument was used for some seven years nearly continuously for the purpose of monitoring the B, C, N and O Lyman-α lines. The measured signals are strongly dependent on the plasma conditions, especially the density and impurity content. Typical count rates for carbon are 50 kHz in L-modes and 200 kHz in H-modes. The oxygen count rates can exceed the carbon count rates in H-modes, even though they are lower in L-modes.

4.1. Spectral survey

In a demonstration experiment a spectrum over the full range was built up in a series of reproducible discharges in L-mode with the following parameters: $B_T = 1.43$ T, $I_p = 400$ kA, $\langle n_e \rangle \approx 5 \times 10^{19}$ m^3, $R = 0.89$ m, $a = 0.24$ cm, elongation $\kappa = 1.5$, $T_e(0) \approx 600$ eV. The discharges were limited on the carbon tiles covering the high field side of the vessel inner wall. The results indicated by open circles in figure 4 are averages over the 1 s flat-top of the

discharges and show clear peaks at the energies of the Kα lines of B IV (206 eV), C V(308 eV) and O VII (574 eV) and the Lyman-α lines of B V (255 eV), C VI (367 eV) and O VIII (654 eV). The boron detected was a remnant from a previous boronization. No nitrogen or iron lines were identified.

The main lines were revisited a few days (70 discharges) after a fresh boronization (+ symbols in figure 4). Unfortunately these discharges were not very reproducible and not identical to those of the spectral scan. Oxygen signals were reduced by a factor of ∼3, carbon signals by a factor of 2–4 and boron was enhanced by a factor of ∼3.

4.2. Estimates of absolute impurity densities and effective charge

Estimates of absolute impurity concentrations directly from these measurements are difficult not only because of uncertainties in the throughput, but also because the ionization balance depends on the transport parameters, which are not known. Calculations using the steady-state ionization equilibrium code IONEQ [11] (see [12] for atomic physics data used in IONEQ). show that the line brilliances vary by a factor of 4, depending on the values assumed for the impurity diffusion coefficient in the range 0.5–2 $\mathrm{m^2\,s^{-1}}$. Hence even an absolutely calibrated USX spectrometer could not provide reliable estimates of impurity densities based on line measurements alone. However, the dependence of the main line Kα and Lyman-α brilliances on D is similar for all four light impurities investigated here, which allows estimation of their relative proportions. Estimates of impurity densities can therefore be obtained when measurements using the USX spectrometer are combined with absolutely calibrated soft x-ray measurements from the core.

When the impurity proportions are known, their absolute densities and hence Z_{eff} can be calculated as in [12]. TCV is equipped with several x-ray systems, including a calibrated 200-channel x-ray tomography system, which uses 47 μm thick beryllium filters, cutting out all radiation below 1 keV in energy [13, 14]. The advantage of using soft x-rays is that they are produced in the hot core, where light impurities are within a few per cent of being fully ionized, independent of impurity transport. In this situation, the volume emissivity, E_z ($\mathrm{W\,m^{-3}}$), which is the sum of line radiation, recombination radiation and Bremsstrahlung over all ionization stages of the ion species of atomic charge z, is given by $E_z = n_{\mathrm{e}} n_z \varepsilon_z(T_{\mathrm{e}})$, where ε_z depends only on the electron temperature. The local soft x-ray emission parameter, ε_z ($\mathrm{W\,m^3}$) is tabulated as a function of electron temperature for each species, Z, of interest from the results of IONEQ coronal equilibrium calculations without transport, taking into account the spectral sensitivity of the detector/filter combination used.

This method has been implemented on TCV both in a local version based on tomographically inverted x-ray profiles as in [12] and as a line-averaged calculation, which makes the assumption of a flat profile of impurity concentration ($n_z/n_{\mathrm{e}} = \mathrm{const}$). For the latter, the soft x-ray brilliance can be written as

$$\Phi^X_{\mathrm{tot}} \equiv \sum_z \Phi^X_z \equiv \frac{1}{4\pi} \int n_{\mathrm{e}}\,\mathrm{d}l \sum_z n_z \varepsilon_z(T_{\mathrm{e}}) = \frac{1}{4\pi} \sum_z \frac{n_z}{n_{\mathrm{e}}} \int n_{\mathrm{e}}^2 \varepsilon_z(T_{\mathrm{e}})\,\mathrm{d}l, \qquad (1)$$

where the integral follows the line of sight of the collimated x-ray detector.

If the relative proportions of impurities, defined as $p_z \equiv n_z / \sum_{\xi \neq b} n_\xi$, are known, the effective charge can be calculated using charge neutrality and assuming full ionization. To this effect we introduce the integrals $\varphi_z = (1/4\pi) \int n_{\mathrm{e}}^2 \varepsilon_z(T_{\mathrm{e}})\,\mathrm{d}l$ and the overall impurity concentration $c_{\mathrm{imp}} \equiv \sum_{\xi \neq b} c_\xi = \sum_{\xi \neq b} n_\xi / n_{\mathrm{e}}$, and express the x-ray brilliance

as $\Phi^X_{\rm tot} = \Phi^X_b + \sum_{z\neq b} \Phi^X_z$, where b is the main ion charge (normally 1), obtaining

$$\Phi^X_{\rm tot} = \left(1 - c_{\rm imp} \sum_{z\neq b} p_z z\right) \frac{\varphi_b}{b} + c_{\rm imp} \sum_{z\neq b} p_z \varphi_z. \tag{2}$$

Since from charge neutrality

$$Z_{\rm eff} = b + \sum_{z\neq b} z(z-b)\frac{n_z}{n_{\rm e}} = b + c_{\rm imp}\left\{\sum_{z\neq b}(z-b)zp_z\right\},$$

we obtain the following expression for the line average effective charge:

$$\bar{Z}_{\rm eff} = b + \frac{\sum_{z\neq b}(z-b)zp_z(b\Phi^X_{\rm tot} - \varphi_b)}{\sum_{z\neq b} p_z(b\varphi_z - z\varphi_b)}. \tag{3}$$

The φ_b integrals are calculated from the tabulated ε_z and the locally measured $n_{\rm e}$ and $T_{\rm e}$, and $\Phi^X_{\rm tot}$ is obtained from the x-ray brilliance measurement. Electron temperatures and densities are obtained from a repetitively pulsed (up to 60 pulses $\rm s^{-1}$) Thomson scattering (TS) diagnostic, which provides measurements every 4 cm along a vertical chord at $R = 0.9$ m [15]. The φ_z integrals are evaluated along an x-ray chord following the Thomson measurement chord to minimize errors of mapping the TS measurements onto the x-ray viewing line. (For the vast majority of plasmas in TCV the x-ray emitting region is entirely within the TS coverage area, obviating the need for mapping).

The role of the USX spectrometer measurements is to provide the impurity proportions in equation (3), the evaluation of which are relatively insensitive to assumptions on transport levels. It has been shown that, as long as only light impurities are involved, the determination of $Z_{\rm eff}$ from x-rays is also not too sensitive to errors on the assumed impurity proportions [12]. These proportions are calculated by modelling the USX line emission using the ionization equilibrium code IONEQ or STRAHL, assuming $D = 1\ \rm m^2\ s^{-1}$ (a typical value consistent with particle transport in many devices [16–24]) and an inward pinch, υ, such that $\upsilon/D = \nabla n_{\rm e}/n_{\rm e}$, which amounts to assuming that the impurity concentration, $n_z/n_{\rm e}$, is independent of the radial position. As shown in section 5.2, the results are not too sensitive to the assumptions on υ/D. The impurity proportions are obtained by normalizing the modelled line brilliances to the measured ones.

Figure 5 shows the evolution of the impurity proportions (top) and concentrations $c_z = n_z/n_{\rm e}$ (middle) and the effective charge (bottom), calculated as above in a series of otherwise reproducible diverted discharges following a boronization (not the same as in figure 4). On the first discharge after a boronization, carbon levels are reduced by a factor of 10 and oxygen levels by a factor of 2–3, while boron accounts for more than 90% of the light impurities. Over the subsequent 10–20 discharges, the carbon and boron concentrations return to their preboronization levels ($\sim$1%), while the oxygen levels continue to drop further to about 0.1%. After this phase the oxygen levels remain low for hundreds of discharges [25].

Figure 6 shows results from Ohmic limiter L-mode discharges, the confinement properties of which have been presented in detail elsewhere [26]. The discharges in the figure include a variety of plasma shapes ($1.4 \leqslant \kappa_{95} \leqslant 1.7$, $0 \leqslant \delta_{95} \leqslant 0.5$), plasma currents ($120 \leqslant I_{\rm p} \leqslant 500$ kA) and densities ($3\times10^{19} \leqslant \langle n_{\rm e}\rangle \leqslant 9\times10^{19}\ \rm m^{-3}$). The parameter that is best correlated with the radiated fraction, $P_{\rm rad}/P_{\rm oh}$, appears to be the electron temperature just inside the LCFS (figure 6(*a*)). The radiated power was measured using three horizontally

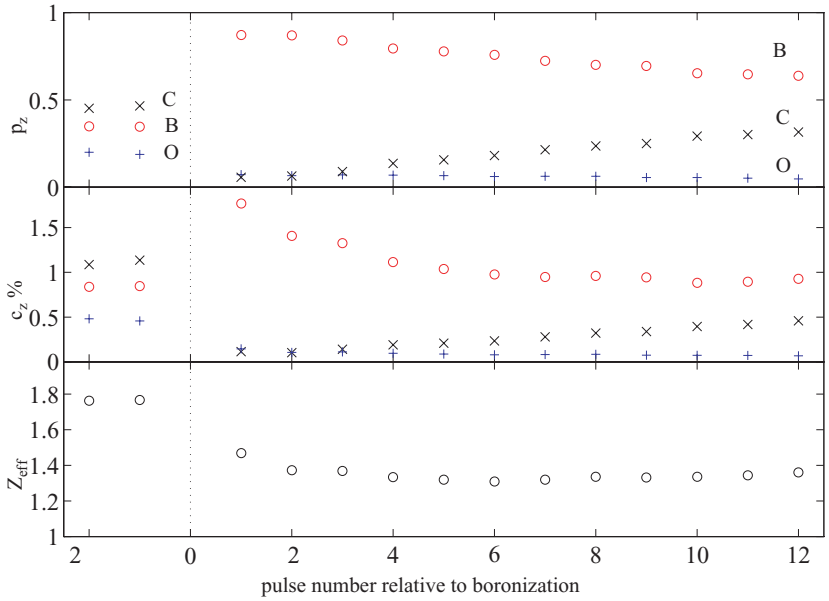

Figure 5. Evolution of light impurity proportions, concentrations and Z_{eff} following a vessel boronization.

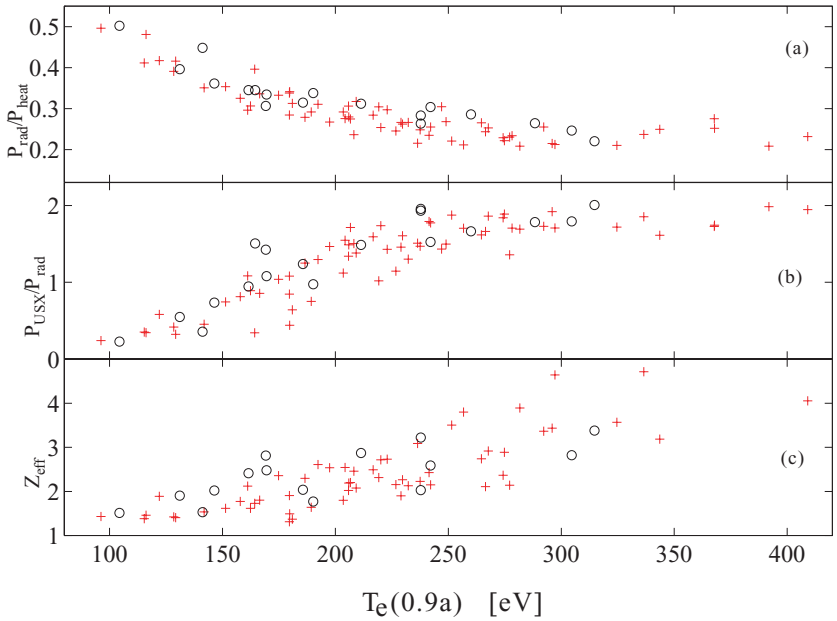

Figure 6. (*a*) Dependence of radiated power fraction (*a*) on edge electron temperature measured at $r/a = 0.9$. (*b*) Fraction of total power radiated by Kα and Lyman-α B, C and O lines in the spectrometer spectral range, obtained by extending the line brilliance measurement by modelling. (*c*) Dependence of Z_{eff} on edge temperature. Symbols refer to classes of triangularity (+, $\delta > 0.2$; ○, $0 < \delta < 0.2$).

viewing bolometer cameras equipped with 16-element arrays of gold foil bolometers. The different symbols refer to low and high plasma triangularity. The edge temperature is itself well correlated with the heat flux per particle [26]. The USX measurements were used to estimate the total power radiated by H and He-like stages of the light impurities by means of IONEQ calculations. The ratio of the calculated power to the total radiated power inferred from bolometry is shown in figure 6(*b*). It rises sharply up to $T_e(0.9a) = 200\,\mathrm{eV}$ and is fairly constant for $T_e(0.9a) > 200\,\mathrm{eV}$. IONEQ calculations show that above this temperature the He and H-like ionizations stages are the dominant contributors to the total radiated power. The mismatch shows that the radiated power from USX measurements is overestimated by a factor of 2, which is within the errors of the measurement (a factor of 2 for the USX spectrometer alone) and of the modelling, which crudely assumed $D = 1\,\mathrm{m^2\,s^{-1}}$ and $\upsilon/D = \nabla n_e/n_e$, irrespective of plasma conditions and impurity species. Figure 6(*c*) shows how Z_{eff} increases with edge temperature, presumably due to the dependence of the sputtering yield on particle energy.

5. Estimates of impurity diffusivities from measurements of the radial profiles of C VI and C V line emission

By monitoring impurity line radiation along many different appropriately distributed lines simultaneously, it is in principle possible to obtain a complete radial profile of the line emission, which can be modelled using a transport code for derivation of the impurity transport coefficients. An opportunity to test the feasibility of such a measurement arose when a more advanced broadband VUV survey spectrometer became available on TCV. The USX spectrometer was no longer required for impurity monitoring and was reoriented such that the four channels could be used for a coarsely resolved radial distribution measurement (figure 7).

5.1. Radially resolved line profile measurements

For this purpose all four channels of the reoriented spectrometer were equipped with MLMs for the carbon energy range. In the usual TCV plasma configurations, the radial distribution of the repositioned four channels of the USX spectrometer still covers only 40% of plasma radius and there is normally no chord that sees the plasma edge where the line radiation profile of light impurities has maximum changes. These circumstances, as well as uncertainties in the relative calibration of the spectrometer channels, do not allow a measurement of the line emission profiles in such plasmas.

Fortunately, the shaping capability of the TCV tokamak allows us to slowly compress a plasma towards the HFS inner wall, thereby sweeping the low field side flux surfaces across the USX viewing lines with good spatial resolution in a single discharge. Such experiments were performed in several Ohmic L-mode limited discharges with plasma currents, I_p, ranging between 130 kA and 300 kA, line averaged electron densities in the range $2 \times 10^{19} \leqslant \langle n_e \rangle \leqslant 6 \times 10^{19}\,\mathrm{m^{-3}}$, central electron temperatures about 700–1100 eV, average elongation $\kappa \sim 1.25$ and average triangularity $\delta \sim 0.25$. The plasmas were compressed by some 10% while keeping q_{95} constant. Examples of the temporal behaviour of the current, safety factor and signals (smoothed) from digital counters of the USX in the discharge with $\langle n_e \rangle \sim 3 \times 10^{19}\,\mathrm{m^{-2}}$ are shown in figure 7. All four channels measured C V radiation at 308 eV. The contours of the LCFSs before the start of the compression and the final LCFS contour at the end of the compression, when the plasma current is minimal, are shown in figure 7 at the right. The vertical lines indicate the lines of sight of the spectrometer. During the 300 ms of compression, each channel scans about 4 cm in the radial direction, resulting in 80% coverage of the distance

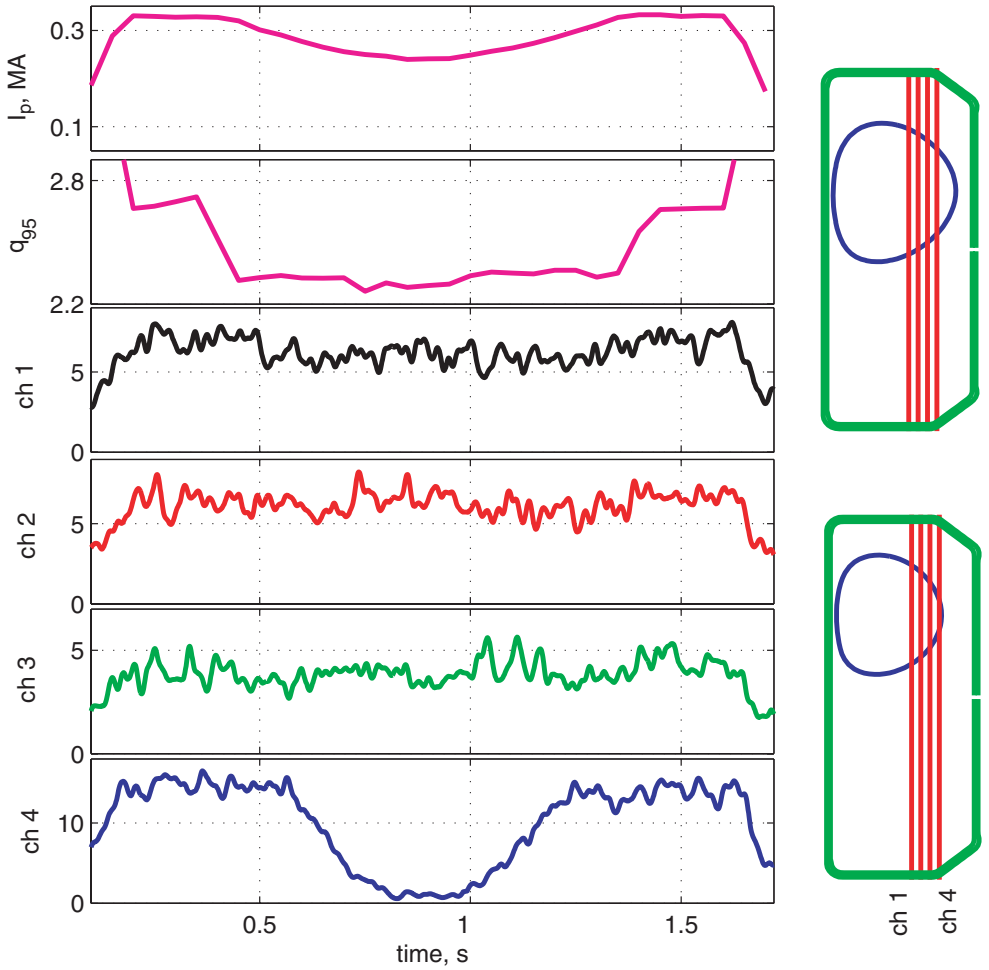

Figure 7. On the left: plasma current, edge safety factor and time traces from digital counters of USX in TCV discharge #24429. On the right: contours of LCFS (blue, dark grey in the printed journal) and the position of the USX chords (red, mid grey in the printed journal) before compression and after maximum compression.

from the plasma centre to the low field side edge for the four channels. It is seen that at the end of the compression the plasma edge is resolved up to the LCFS and the signal of the detector closest to the edge drops practically to zero. The signal fluctuations can be explained by poor photon statistics due to a short integration length just inside the LCFS.

In order to derive a steady-state profile of line emission, the main plasma parameters such as the density and safety factor profiles were kept as constant as possible during the compression. It was assumed that current changes during the compression do not significantly affect the impurity transport parameters as long as the edge safety factor remains constant [27].

Due to the relatively short distance between channels, plasma positions as measured by the poloidal flux based normalized minor radius $\rho_{\mathrm{pol}} = \sqrt{\psi/\psi_{\mathrm{LCFS}}}$, seen by one channel at the beginning of the compression pass in front of the neighbouring channel at the end of the compression. This overlap allowed us to make a relative calibration of the channels,

linking the values of the signal at different stages in the compression. It is essential for such a cross-channel calibration that the total impurity concentration during the compression remains constant. This was indeed ascertained using Z_{eff} derived from soft x-rays as described in section 4. To correctly connect the signals from neighbouring channels one should also take into account the changes in integration length during the sweep. To do so, signals from each channel were renormalized by the corresponding path length inside the LCFS at each time. The resulting normalized profile obtained from USX measurements at 308 eV is shown in figure 8 as a function of the impact parameter (smallest value of ρ_{pol}) of the viewing line. The different symbols correspond to the different channels of the spectrometer. In the plasma compression phase presented here, the signal of each chord starts at lower values of ρ_{pol} and goes to the right in ρ_{pol} as the plasma becomes smaller.

5.2. Modelling of the emission profiles

The profile shown above was deemed to represent a steady-state line integrated emission profile of C v and was used to obtain carbon transport parameters using the STRAHL code [28]. STRAHL is a one-dimensional transport code that calculates the solution of the equation of impurity particle conservation for each ionization stage,

$$\frac{\partial n_{I,Z}}{\partial t} = -\nabla \vec{\Gamma}_{I,Z} + Q_{I,Z},$$

where $\Gamma_{I,Z}$ is the flux density of the impurity and $Q_{I,Z}$ is the source/sink term, which includes ionization, radiative, dielectronic and charge exchange recombination from and to the neighbouring ionization stages. The impurity flux density was represented in the conventional form as a sum of diffusive and convective terms:

$$\Gamma_Z = -D\nabla n_Z + \upsilon n_Z.$$

The background electron temperature and density profiles used in the simulations were taken from the TS system and mapped onto the ρ_{pol} grid using the equilibrium code LIUQE [29]. The modelling included profiles of D and υ as a function of ρ_{pol} as input parameters and the line brilliance as an output. The line emission profiles from the simulation were then mapped onto the real discharge geometry and integrated along each USX chord. Line integrals were normalized to the corresponding chord length in order to follow the same procedure as for the experimental profile in figure 8. The resulting profiles were compared with experimental ones in order to find the D and υ that give the best fit. To this effect the profiles of D and υ were given by smoothly connecting five nodal points along the minor radius. The best fitting ones were found iteratively, by independently scanning the node values.

In figure 9 (left) the experimental profile of integrated line emission measured by USX (dots) is plotted together with the simulated one (line), showing good agreement between experiment and simulation for the C v line at 308 eV. We obtain consistent results when using the C vi line at 368 eV, as shown in figure 10 for an identical discharge (#24426).

The examples of radial profiles of the diffusion coefficients used in simulations are shown in figure 9 on the right and produce indistinguishable results. It was found that there is a range of profiles of the diffusion coefficient that give a good fit to the final profile of integrated line emission. In general, the best fitting profiles of D obey the following rule. The profiles with the highest values of D at the edge are also the ones with the steepest rise (concave profile on figure 9, right). Profiles with a lower value at the edge are associated with a more gradual decay towards the plasma centre. Based on the profiles of D suitable for this discharge, the accuracy in the determination of diffusion coefficient can be estimated at 30% at the edge and

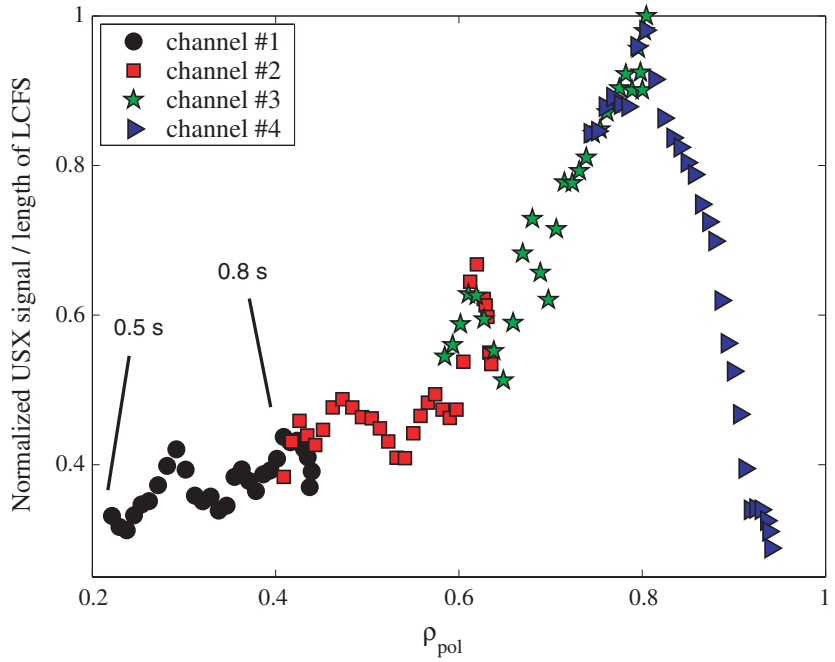

Figure 8. The resulting normalized profile of line emission obtained from USX measurements at 308 eV (He-like carbon) as a function of the impact parameter using the $\rho_{\rm pol}$ flux coordinate. The numbers on the graph correspond to the times of measurement for channel 1 (black dots) at the start and at the end of the sweep.

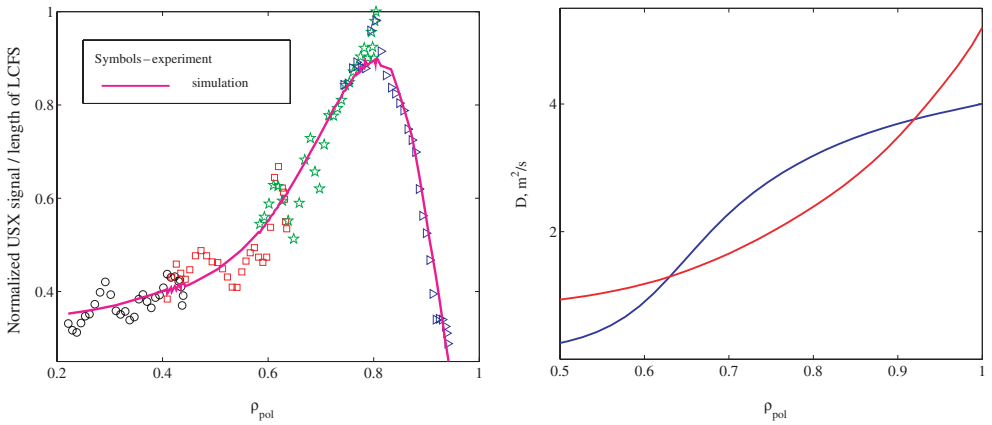

Figure 9. The experimental profile measured by USX (· · · · · ·) is plotted together with the simulated one (——). The same result is obtained by both profiles of diffusion coefficients shown on the right.

70% at $\rho_{\rm pol} \sim 0.6$. The values of D in the region $\rho_{\rm pol} < 0.5$ do not influence the simulated profile.

The results were found to be practically independent of the profile of convective velocity, υ. In the simulations, D was kept fixed, while parabolic profiles for υ were assumed with $\upsilon(0) = 0$ and υ (1) was varied in the range $10\,{\rm m\,s^{-1}}$ to $-10\,{\rm m\,s^{-1}}$. Such variations resulted in changes

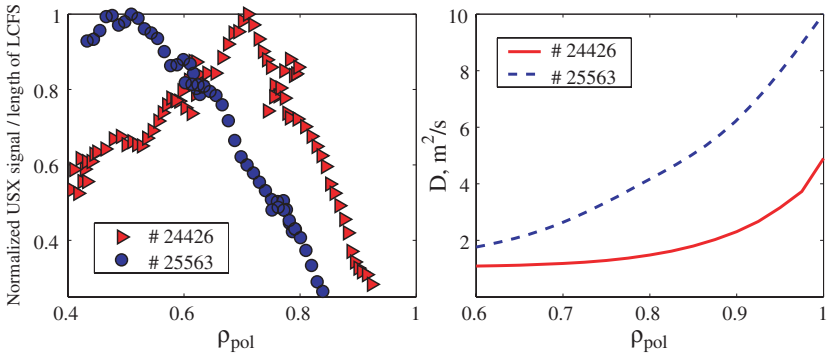

Figure 10. The resulting normalized profiles of line integrated C VI (368 eV, H-like line) line emission mapped on the ρ_{pol} grid obtained from USX measurements in two different discharges with different plasma density. Discharge 24426 was an identical repeat of the discharge shown in figure 9.

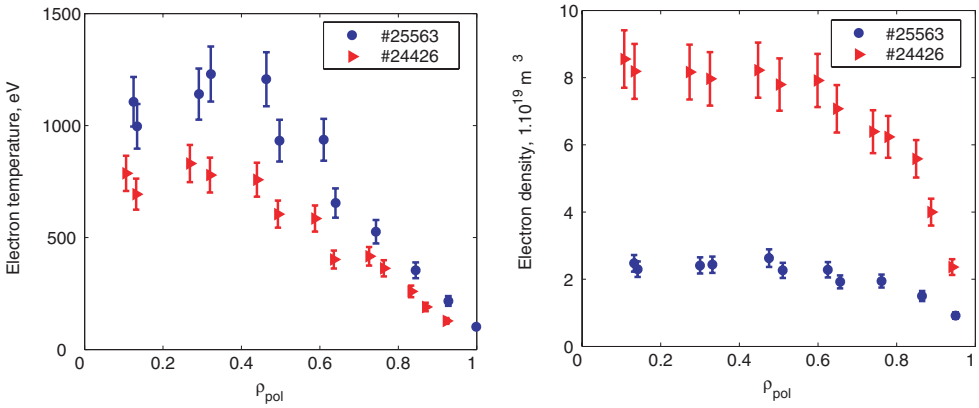

Figure 11. Electron temperature (left) and density profiles from TS for the two discharges shown in figure 10.

in the final integrated profile that are smaller than the experimental uncertainties. The reason could be the dominance of the diffusive part over the convective part in the total particle flux because of large values of C V (or C VI) density gradients distinctive for partly ionized stages in tokamak plasmas. Accordingly, the pinch velocity remains undetermined.

In figure 10 (left), the experimental profiles of integrated emission of the C VI (368 eV) line are presented for two discharges. Discharge #24426 (triangles) has an average plasma current of 270 kA and line average plasma density $\langle n_{\mathrm{e}} \rangle \approx 6 \times 10^{19}\,\mathrm{m}^{-3}$. The second discharge, shown using dots, has the same average plasma current and a significantly lower plasma density $\langle n_{\mathrm{e}} \rangle \approx 2 \times 10^{19}\,\mathrm{m}^{-3}$. The values of the edge safety factor, q_{95}, are the same for both discharges and are equal to 2.2. The temperature was higher in the lower density discharge, $T_{\mathrm{e}}(0) \approx 1.1$ keV, as compared with $T_{\mathrm{e}}(0) \approx 0.8$ keV at the high density, for otherwise similar profile shapes, as shown in figure 11.

The profiles of the integrated line emission (figure 10) for these two discharges are remarkably different. In the case of the lower density discharge, the maximum and the outer gradient region of the profile are displaced towards the plasma centre with respect to the profile in the discharge with higher density. If the transport parameters were the same,

the maximum of the emission profile would be displaced outwards for the low density case, not inwards, as observed. The difference can only be explained by a substantial increase in impurity diffusivity with decreasing density. The simulations reproduce both profiles well, giving, for the low density discharge, best fitting values of D at the edge that exceed by a factor of 2 the values obtained at a higher density (figure 10, right).

6. Discussion

The relationship between particle and heat transport coefficients is a matter for concern in fusion reactors and is theoretically less straightforward than sometimes assumed, even in a two-species plasma [30]. The above profiles of the diffusion coefficient were compared with the profiles of the effective heat conductivity coefficient $\chi = Q_{\mathrm{tot}}/[n_{\mathrm{e}}\langle|\nabla T_{\mathrm{e}}|\rangle]$ obtained from the power balance. In the case of the high density discharge, where χ is of the order of 4 $\mathrm{m}^2\,\mathrm{s}^{-1}$ at the edge, the diffusion coefficient, D, is similar in shape and in magnitude to χ. In the low density case, χ rises to as high as 25 $\mathrm{m}^2\,\mathrm{s}^{-1}$ at the edge. The carbon ion diffusion coefficient is higher than in the high density case as well, but does not exceed 10 $\mathrm{m}^2\,\mathrm{s}^{-1}$ at the edge. One can conclude that the carbon diffusion coefficient is not related to the effective heat conductivity coefficient via a simple proportionality coefficient. This conclusion is confirmed by an analysis of several discharges with different values of χ.

A more relevant study should be made using separately determined electron (χ_{e}) and ion (χ_{i}) heat conductivities. Unfortunately, the large uncertainties related to the calculation of conductivities at the edge ($\rho_{\mathrm{pol}} > 0.6$) due to errors in the ion temperature profile and the equipartion term do not allow us to make a reliable analysis. An interesting particularity of the results obtained is that the best fitting values of the diffusion coefficient in these experiments are higher by a factor of 5 than the values typically obtained for silicon impurities introduced by laser ablation [23]. The reason for this discrepancy remains unknown, although it should be noted that the laser ablation experiments, which are analysed using soft x-ray diagnostics in different discharges, only provide information for $\rho < 0.8$, whilst the transport parameters from the experiments described in this paper are characteristic of the plasma periphery, $\rho > 0.6$.

7. Conclusions

The use of MLMs in the ultrasoft x-ray region allows measurements of line emission from highly ionized light impurities in a way that is similar to the popular filter methods in the visible wavelength range for lower ionization stages. The throughput of the instrument described was only known from the measurements of its components, resulting in uncertainties of a factor of 2 of the measured absolute line brilliances. This situation could be improved by an absolute throughput calibration using a synchrotron source. Even uncalibrated, the instrument is useful for monitoring changes in the impurity composition of the plasma and for providing the relative proportions of light impurities for a calculation of Z_{eff} from soft x-ray measurements. The spectrometer on TCV was modified for radial emission profile measurements in specially designed radially swept discharges. The results show that the line integrated radial emission profiles provide a significant constraint for determining the diffusion coefficient in the outer part, $\rho_{\mathrm{pol}} > 0.6$, of the discharge. A series of discharges in different conditions show that there is no simple proportionality between the carbon ion diffusion coefficient and the effective heat diffusivity. The currently used instrument was only intended as a feasibility demonstration and is not adapted for routine measurements of the ionization balance. A curved imaging MLM device could provide time resolved radial profiles in every discharge [7–9]. Another possibility

would be localized charge exchange recombination measurements of different ionization stages of carbon, using a diagnostic neutral beam.

Acknowledgments

The authors wish to thank R Dux and A Weller for making their ionization equilibrium codes available. This work was partly supported by the Fonds National Suisse de la Recherche Scientifique and by the Academy of Science of the Czech Republic, Grant K 204 31 05.

References

[1] Moos W, Zwicker A P, Regan M and Finkenthal M 1990 *Rev. Sci. Instrum.* **61** 2786
[2] Zwicker A P *et al* 1992 *Rev. Sci. Instrum.* **63** 5037
[3] Regan S P *et al* 1997 *Rev. Sci. Instrum.* **68** 1002
Regan S P *et al* 1997 *Rev. Sci. Instrum.* **68** 732
[4] Carraro L *et al* 1997 *Rev. Sci. Instrum.* **68** 1043
[5] Soukhanovskii V A *et al* 2001 *Rev. Sci. Instrum.* **72** 737
[6] Duorah S *et al* 2001 *Rev. Sci. Instrum.* **72** 1183
[7] Stutmann D *et al* 2001 *Rev. Sci. Instrum.* **72** 732
[8] Shmaenok L A *et al* 2001 *Rev. Sci. Instrum.* **72** 1411
[9] Piffl V, Badalec J and Weinzettl Vl 1999 *26th EPS Conf. on Controlled Fusion and Plasma Physics (Maastricht(NL), June 1999)* vol 23J (Europhysics Conference Abstracts) p 1605
[10] MOXTEK Inc., Orem 452W 1260N, Utah 84057, USA
[11] Weller A *et al* 1987 *JET Report* JET-IR(87)10
[12] Weisen H, Pasini D, Weller A and Edwards A W 1991 *Rev. Sci. Instrum.* **62** 1531
[13] Anton M *et al* 1995 *Rev. Sci. Instrum.* **66** 3762
[14] Anton M *et al* 1996 *Plasma Phys. Control. Fusion* **38** 1849
[15] Behn R *et al* 1995 *Proc. 7th Int. Symp. Laser Aided Plasma Diagnostics (Fukuoka)* p 392
[16] Pasini D *et al* 1992 *Plasma Phys. Control. Fusion* **34** 677
[17] Regan S P *et al* 1997 *Nucl. Fusion* **37** 657
[18] Rice J E *et al* 1997 *Phys. Plasmas* **4** 1605
[19] Mattioli M *et al* 1998 *Nucl. Fusion* **38** 189
[20] Dux R 1999 *Nucl. Fusion* **39** 1509
[21] Dux R and Peeters A G 2000 *Nucl. Fusion* **40** 1721
[22] Dux R 2003 *Fusion Sci. Technol.* **44** 276903
[23] Scavino E *et al* 2003 *Plasma Phys. Control. Fusion* **45** 1961
[24] Scavino E *et al* 2004 *Plasma Phys. Control. Fusion* **46** 857
[25] Pitts R A *et al* 1997 *J. Nucl. Mater.* **241–243** 867
[26] Weisen H *et al* 1997 *Nucl. Fusion* **37** 1741
[27] Zabolotsky A, Weisen H and TCV Team 2003 *Plasma Phys. Control. Fusion* **45** 735
[28] Dux R *STRAHL User Manual* IPP Garching, Germany, http://www.rzg.mpg.de/∼rld/strahl.ps
[29] Hofmann F *et al* 1988 *Nucl. Fusion* **28** 1871
[30] Baker D R *et al* 1998 *Nucl. Fusion* **38** 485